ITC 2/54
Information Technology and Control
Vol. 54 / No. 2/ 2025
pp. 695-711
DOI 10.5755/j01.itc.54.2.40643

WNASNet: Wavelet-Guided Neural Architecture Search for Efficient Single-Image De-raining

Received 2025/02/25 | Accepted after revision 2025/04/28

HOW TO CITE: Tao, W., Chen, Q., Yu, C. (2025). WNASNet: Wavelet-Guided Neural Architecture Search for Efficient Single-Image De-raining . *Information Technology and Control*, 54(2), 695-711. https://doi.org/10.5755/j01.itc.54.2.40643

WNASNet: Wavelet-Guided Neural Architecture Search for Efficient Single-Image De-raining

Wenyin Tao, Qiang Chen, Chunjiang Yu

School of Intelligent Management; Suzhou Industrial Park Institute of Services Outsourcing; Jiangsu, China
wenyin.tao@gmail.com (T. W.), chenq@siso.edu.cn (C. Q.), yucj@siso.edu.cn (Y. C.)

Corresponding author: wenyin.tao@gmail.com

On rainy days, the uncertainty of the shape and distribution of rain streaks can cause the images captured by RGB image-based measurement equipment to be blurred and distorted. The wavelet transform is extensively utilized in conventional image-enhancing techniques because of its capacity to deliver spatial and frequency domain information and its multidirectional and multiscale characteristics. In image de-raining, the distribution of rain streaks is intricately linked to both spatial domain characteristics and frequency domain spatial attributes. Nonetheless, deep learning-based rain removal models predominantly depend on the spatial characteristics of the image, and RGB data is sometimes insufficient to differentiate rain marks from image details, resulting in the loss of essential image information during the rain removal process. To overcome this limitation, we have created a lightweight single-image rain removal model named the wavelet-enhanced neural architecture search network (WNASNet). This technique isolates image features from rain-affected images and can more efficiently eliminate rain artifacts. The proposed WNASNet presents three notable contributions. Initially, it utilizes wavelet transform to extract multi-frequency feature components. It allocates a distinct feature search block (FSB) to each component, facilitating the identification of task-specific feature extraction networks to enhance deraining efficacy. Secondly, we present a straightforward yet efficient wavelet feature fusion technique (SFF) that selectively employs high- and low-frequency features during the inverse wavelet transformation. This method maintains deraining efficacy while substantially decreasing computational complexity relative to conventional frequency blending techniques. Comprehensive studies on four synthetic and two real-world datasets illustrate the better performance of WNASNet across many evaluation measures, including PSNR, SSIM, LPIPS, NIQE, and BRISQUE, thereby verifying its efficacy and robustness for single-image deraining tasks.

KEYWORDS: Image Deraining, Wavelet Transform, Signal Processing, Neural Architecture Search

1. Introduction

Single-image deraining is a challenging task in computer vision that aims to eliminate rain streaks from images. It has practical applications in domains such as autonomous driving [4], [18] on rainy days and enhancing object detection algorithms [36]. However, the problem of restoring a degraded image [42] containing rain streaks to a clear image is complex due to the unpredictable and dynamic nature of rain streak distribution and orientation within an image.

Conventional image de-raining methods [38], [39] typically rely on hand-crafted features or filters to remove rain streaks. Nonetheless, these methods often need help to handle complex rain streak patterns, resulting in artifacts or loss of image details. With the advancements in deep learning techniques, researchers have started exploring the application of neural networks [17], [41] for image rain streak removal.

In addition to image de-raining algorithms based on spatial characteristics, wavelet transforms based on the frequency domain are widely used mathematical tools in image restoration tasks [12]. Unlike CNN and Transformer-based image restoration networks, wavelet transforms are inherently multi-scale, which allows them to capture coarse-to-fine structures in images, such as edges and textures. In addition, the wavelet transform has good sensitivity to edges, making it possible to preserve edge information during image restoration and reduce blurring and distortion around the edges. These features are particularly important for image restoration tasks. Discrete wavelet transform (DWT) is a wavelet transform used for image processing that decomposes an image into four different sub-images: low-low (LL), low-high (LH), high-low (HL), and high-high (HH). Liu et al. [23] proposed a multi-scale wavelet CNN (MWCNN) model, which constructs a U-Net network structure through DWT and multi-scale image features to improve the performance of the image restoration model. Hsu et al. [10] proposed an image super-resolution enhancement technique that uses the high-frequency sub-images of the stable wavelet transform (SWT) and interpolates the input image to enhance the image boundaries.

Neural architecture search (NAS) has gained significant attention from researchers [3], [22] as a means to automatically discover optimal architectures [2]. These approaches aim to reduce the trial-and-error process and improve upon hand-designed architectures. As a result, NAS has become a crucial area of study in deep learning. Building upon NAS, several methods have been proposed to automate the design of deraining networks [1], [6] using NAS. However, these methods have limitations. Firstly, efficient NAS approaches primarily focus on overall network architectures rather than component cell structures, such as DARTS [22] and β-DARTS [43]. Hence, the optimization is directed towards network architectures instead of component structures. Secondly, searching for the best model architecture is computationally expensive. While various NAS approaches reduce the search space while maintaining performance, the objective remains to identify the best network architecture. This requires significant computational resources to train and validate numerous network architectures, as demonstrated in Liu et al. [20], which took over 100 GPU days to complete.

This paper presents a novel Wavelet Enhanced Neural Architecture Search (WNASNet) method, which conducts neural architecture search on wavelet-transformed image features to obtain a lightweight single-image de-raining model. Our approach explores different combinations of nodes within the search space to identify the optimal network architecture and parameters. We convert input features into high-frequency and low-frequency components by utilizing wavelet transform. We search for a suitable feature extraction network for each feature component that effectively addresses single-image rain removal. The low-frequency feature extraction network restores structural and textural information, while the high-frequency feature extraction network enhances edge details.

Unlike previous NAS-based single image de-raining networks, our proposed WNASNet employs wavelet transform to convert image features into the frequency domain, resulting in four frequency components. De-raining is achieved through feature extraction and restoration of these components. We introduce separate feature search blocks (FSBs) for each frequency component to enhance the network's rain removal capabilities. This allows us to obtain feature extraction networks tailored to the characteristics of different

frequency components. In addition, we experimentally observed that similar recovery effects, resulting in a lighter network, are obtained by using only the high and low-frequency features from the four components. Experimental results show that our method outperforms existing NAS-based single-image rain streak-removing methods on standard benchmarks. In Rain200L, Rain200H, Rain800, and Rain1200 benchmarks, our approach achieves significantly higher PSNR and SSIM values, validating WNASNet' effectiveness, as shown in Figure 1.

The contributions of this study are summarized as follows:

1 Our proposal presents an innovative method called Wavelet Enhanced Neural Architecture Search (WNASNet). This method employs NAS attributes in the frequency domain to investigate the feature extraction network, yielding enhanced picture restoration and a more efficient network architecture.

2 We utilize multiple autonomous Frequency Search Blocks (FSBs) to improve image de-raining and to identify networks suitable for diverse frequency component attributes. Additionally, we have devised a simple feature fusion technique (SFF) that enables the transformation of frequency-domain data into RGB-domain features. This approach reduces the parameter count in the model and improves its inference speed.

3 Experimental results on synthetic and real datasets demonstrate that the proposed WNASNet algorithm offers substantial performance enhancements compared to existing leading approaches.

Figure 1

Single image de-raining on the Rain200L dataset. Our method performs much better than other state-of-the-art algorithms.

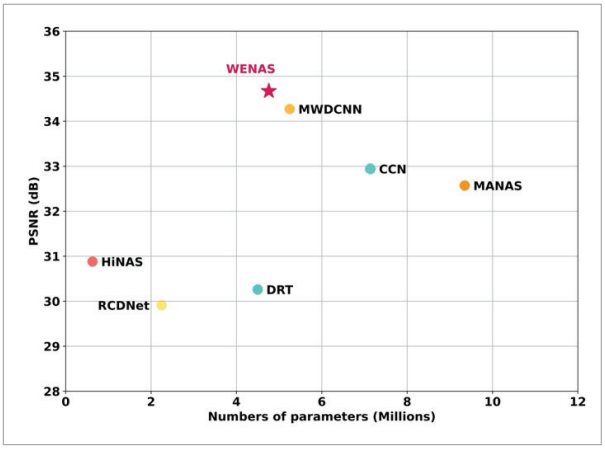

The remaining part of the paper is structured in the following manner. Section 2 provides an overview of relevant research, encompassing conventional techniques for removing rain from images, deep learning approaches for rain removal, and methods that employ neural architecture search for rain removal. Section 3 outlines the proposed WNASNet network, designed to remove rain from single images. Section 4 compares the most advanced techniques, a discussion, and experiments that test the effectiveness of eliminating specific components. Section 5 summarizes the paper's main findings, presents the conclusion, and outlines potential areas for future research.

2. Related Works

2.1. Traditional Image De-raining Methods

Traditional image processing methods for de-raining typically rely on handcrafted features and mathematical models. These methods often assume specific degradation models, such as rain streaks being modelled as a combination of low-rank [5] and sparse matrices [25]. Based on these assumptions, various algorithms [5] have been developed to separate rain streaks from the clean background.

One popular approach is based on the non-local means (NLM) filter [14], which exploits the redundancy in rain streaks to remove them. The NLM filter estimates the similarity between image patches and uses this information to perform denoising and de-raining. Another commonly used method is the guided filter [28], which uses information from a guidance image to guide the de-raining process. These methods have achieved promising results in de-raining tasks by effectively exploiting the relationships between rain streaks and clean backgrounds.

Traditional de-raining methods often rely on handcrafted features and heuristics, which cannot capture the diverse rain patterns adaptively. These methods also need more generalization capability, as they are designed based on specific assumptions about rain characteristics. As a result, they may not perform well when the rain patterns deviate from the assumptions, leading to unsatisfactory de-raining results.

2.2. Deep Learning-based De-raining Networks

Recent advancements in deep learning methodologies have yielded substantial successes in various computer vision applications [45], including de-raining. These methods leverage the formidable capacity of deep neural networks to comprehend the correlation between rainy photographs and their corresponding clear counterparts. Convolutional Neural Networks (CNNs) [32] have been extensively utilized for de-raining tasks. The networks are trained with pairs of rainy and clear photos to reduce the difference between the network's output and the actual clear image. CNN-based de-raining methods have achieved superior visual quality and quantitative metrics performance through huge datasets and sophisticated network architectures.

Deep residual networks [9] are especially appropriate for sophisticated visual applications. In their research, Fu et al. [7] introduced a novel deep detail network (DDN) employing a sequential network [51] design to enhance the efficacy of rain removal inside the model. Unlike the study conducted by Fu et al., Ren et al. [31] introduced a straightforward and efficient asymptotic rain removal network. Parameter sharing is implemented at various phases to execute image deterioration and reduce the number of model parameters. The fundamental objective of low-level visual tasks is to enhance the quality of input images for advanced visual tasks. The velocity of executing fundamental visual activities influences the efficacy of intricate visual tasks. Consequently, Fu et al. [8] introduced the lightweight de-raining network (LPNet). The image restoration technique entails extracting several levels of detail from the image through the feature pyramid structure and the residual structure. The RESCAN methodology proposed by Xia et al. [17] seeks to enhance the efficacy of the progressive de-raining network by discerning correlations among multi-scale image elements.

While CNN networks can autonomously acquire knowledge about rain streaks, creating a network architecture that is both effective and efficient remains difficult. The network's performance is primarily determined by the architecture's capacity to accurately capture low-frequency rain patterns and scene details without succumbing to overfitting or excessive model complexity.

2.3. Neural Architecture Search

The goal of NAS is to autonomously discover neural network architectures using advanced search techniques such as Evolutionary techniques (EA), Reinforcement Learning (RL), Gradient-Based Algorithms, etc., instead of manually building them. The objective is to explore a range of potential networks by employing an optimization method. The space of possible networks can be generated by reparameterization or by utilizing a pre-established collection of network architectures. The optimization approach usually entails assessing the performance of potential networks on a validation set and adjusting the network parameters based on gradients calculated for the validation loss. Liu et al. [21] employed evolutionary algorithms to iteratively and mutatively tune neural network designs and parameters within a pool of candidate architectures. Zoph et al. [52] employed reinforcement learning to explore neural network structures within a predetermined search domain. Nevertheless, neural architecture searches that rely on reinforcement learning and evolutionary algorithms necessitate revision to mitigate issues such as prolonged search durations. Liu et al. [22] developed a differentiable neural architecture search (DARTS) that relies on gradients. The method enhances the efficiency of the search process by including differentiability and subsequently employing shared parameters to decrease the search space and expedite the search process. Neural architecture search methods have facilitated the conduction of multiple investigations on picture reconstruction. Suganuma et al. [33] developed the E-CAE technique for image restoration. This approach is the pioneering network that employs NAS for image restoration. The network uses evolutionary algorithms to discover a network design based on self-encoding. Zhang et al. [46] introduced Hierarchical NAS (HiNAS) as a method for picture denoising. The approach utilizes a network search algorithm that relies on gradients and constructs a hierarchical search space featuring adaptive sensory fields. Lee et al. [15] introduced Denoising Prior Neural Architecture Search (DPNAS) as a method specifically designed for image denoising. The approach prioritizes the exploration of superior components rather than the exploration of the entire network architecture. Consequently, the search

space size is diminished, leading to an enhancement in search efficiency. In contrast to the methods above, we convert the input image from the RGB color space to the frequency domain space. Subsequently, NAS is employed to explore the network architecture within the frequency domain space to identify a neural network that exhibits exceptional performance in the task of picture de-raining.

3. Method

The aim of this study is to separate the features of the input image into high-frequency features and low-frequency features using a wavelet transform. Each feature component is assigned to a separate Neural Architecture Search (NAS) to find a feature extraction network that matches the component. Finally, a clean image is recovered from a wet image using feature fusion and an image reconstruction network. In Section 3.1, we present the structure of the WNASNet approach, used for de-raining single images. Next, the Feature Search Block (FSB) implementation is presented in Section 3.2. Section 3.3 presents a detailed analysis of the design concepts and features of the Frequency Feature Fusion Block. Section 3.4 introduces the approach and the loss function used for image reconstruction.

3.1. Network Architecture

Rain streaks in rain images exhibit a variety of shapes, sizes, and orientations, rendering them indescribable using a singular pattern. Furthermore, rain streaks have the potential to partially obstruct structural and detailed information in the background of the image, resulting in the loss of crucial data. In order to tackle these difficulties, this work proposes an approach that integrates wavelet theory with neural architecture search. The objective is to surmount these problems and enhance the effectiveness of rain removal in single images. The input image data in this study are initially transformed from the RGB domain to frequency domain information using Discrete Wavelet Transform (DWT). Next, the feature extraction network is queried for various feature components using a feature search block (FSB). Subsequently, the feature extraction network applies inverse wavelet transform (IWT) to the various extracted features, employing a straightforward feature fusion approach (SFF) to obtain the picture features in the RGB domain. Ultimately, a network for picture restoration produces a clear image devoid of rain streaks, as illustrated in Figure 2.

More precisely, when provided with a deteriorated image $I_r \in R^{3\times H\times W}$, WNASNet first utilizes two convolution layers to produce a shallow feature map

Figure 2

The WNASNet design comprises five components: a shallow feature extraction network, a wavelet transform block, a feature search network, a wavelet feature fusion block, and an image recovery network.

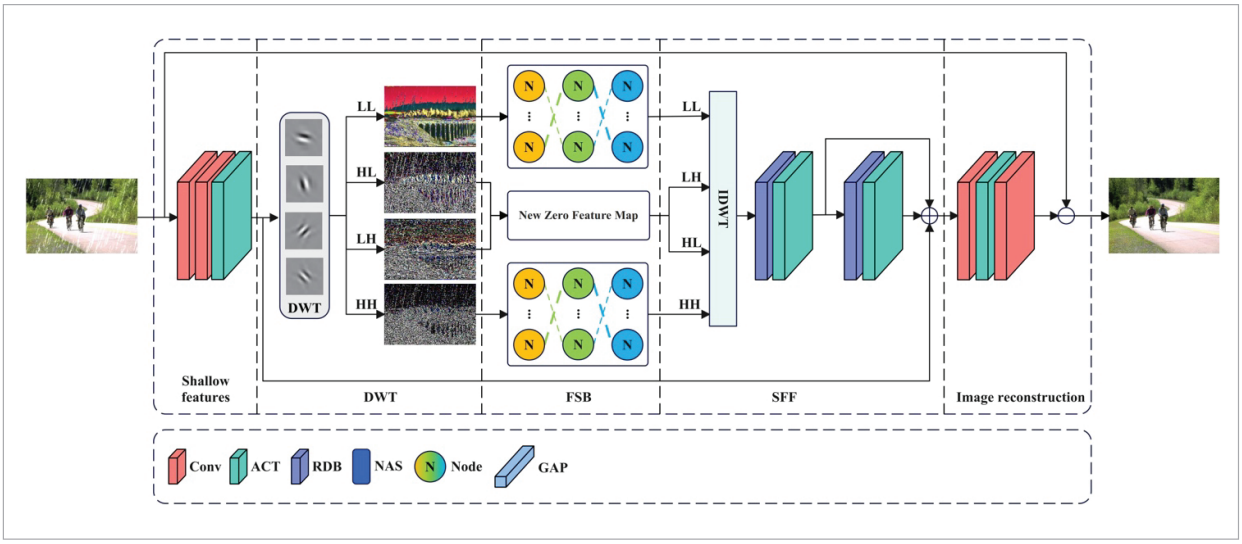

$X_0 \in R^{C\times H\times W}$. Here, C indicates the number of channels and $H\times W$ represents spatial locations. The shallow features are transformed into four components using 2D-DWT. These components are denoted as low-low component (X_{LL}), low-high component (X_{LH}), high-low component (X_{HL}), and high-high component (X_{HH}). It is worth noting that X_{LL} represents the structural information of the image. The details and edges of the image are denoted as X_{LH}, X_{HL} and X_{HH}. The initial step involves horizontally decomposing the input feature map X_0 using high-pass and low-pass filters. This decomposition yields the low-frequency component $X_L \in R^{C\times H\times \frac{W}{2}}$ and the high-frequency component $X_H \in R^{C\times H\times \frac{W}{2}}$. Subsequently, the features $[X_L, X_H]$ acquired in the preceding stage are vertically decomposed by employing a high-pass filter and a low-pass filter. This decomposition process yields the complete components $X_{DWT} = [X_{LL}, X_{LH}, X_{HL}, X_{HH}] \in R^{C\times \frac{H}{2}\times \frac{W}{2}}$ of the input feature map X_0. Due to the utilization of interval sampling in the decomposition process, the width and height of the output features are reduced to half of the dimensions of the input features, as depicted in Figure 3.

After the wavelet transform is completed, the FSB module searches for a suitable feature extraction network using NAS for the feature components, e.g., $X_{N_{LL}} = f_{NAS}(X_{LL})$. The shape of the output features of each FSB module is the same as the shape of the input features.

It is proved that the feature components obtained after using wavelet transform are not independent but potentially correlated. Therefore, we use a simple feature fusion (SFF) method to fuse the different feature components according to a rule to obtain new feature components. In this process, we first create two feature maps ($X_{N_{HL}}$ and $X_{N_{LH}}$) with both feature values of zero, which have the same shape as the shape of the output feature map of the FSB block. Finally, 2D-IWT is used to recover $X_{N_{LL}}$, $X_{N_{HH}}$, $X_{N_{HL}}$ and $X_{N_{LH}}$ as image features $X_F \in R^{C\times H\times W}$ in RGB domain.

Figure 3

The procedure of 1-level 2D-DWT decomposition.

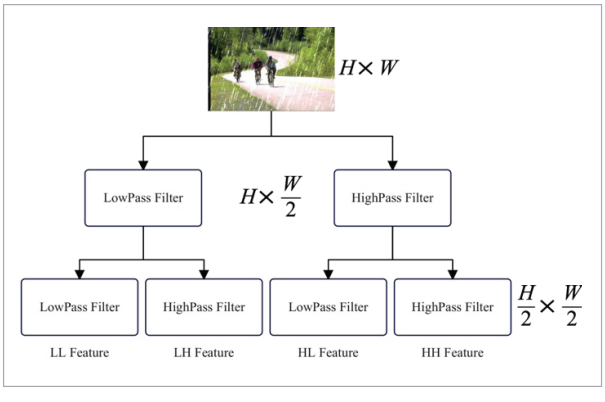

Table 1

The Rain200L dataset evaluated the time complexity with the same hardware settings as the six comparison models. The higher the FPS, the less GPU time the model uses and the more efficient it is. The color **red** signifies the highest level of performance.

Methods	Publication	FPS	Params (MB)
HiNAS [47]	CVPR' 2020	26.60	0.63
RCDNet [36]	TNNLS' 2023	1.40	2.25
CCN [29]	CVPR' 2021	0.53	7.14
DRT [19]	CVPRW' 2022	0.60	4.50
MWDCNN [35]	PR' 2023	4.26	5.25
MANAS [1]	TCSVT' 2023	2.31	9.35
Ours		**96.47**	4.76

After the inverse wavelet transforms, the image feature X_F passes through two RDB modules to obtain $X_{RDB} \in R^{C\times H\times W}$. The RDB [34] modules achieve more detailed feature enhancement. Finally, the rain streak $R = Conv(X_{SE}) \in R^{3\times H\times W}$ is obtained by a 5×5 convolution layer in the image reconstruction network, and the reconstructed image I_{clr} is obtained using the image degradation model $I_{clr} = I_r - R$.

The computational complexity of WENAS was evaluated on NVIDIA GeForce RTX 3090, showing a significant reduction in GPU time compared to six comparative models, which underscores its efficiency, with the results shown in Table 1.

3.2. NAS-based Feature Search Block

In order to improve the efficiency of NAS search, the topology and node search of NAS cells is performed using the gradient-based search using differentiable architecture sampler (GDAS) method [3]. Each cell is regarded as a directed acyclic graph (DAG) with N nodes. Each cell has two inputs, J_n^1 and J_n^2, where J_n^1 is the output of the $(n-1)$-th cell and J_n^2 is the output

of the (n–2)-th cell. In the n-th cell, two operations, O_n^1 and O_n^2, are applied to the input feature maps J_n^1 and J_n^2, respectively, and then the output after O_n^1, O_n^2, is concatenated, and a 1×1 convolution operation is performed to produce the output feature map J_n, as depicted in Figure 4. The mathematical expression is as follows:

$$I_n = Cov_{1\times1}\left(concat\left(O_n^1(I_n^1), O_n^2(I_n^2)\right)\right) \quad (1)$$

The Node in Figure 4 represents the operation in the cell. By learning, the NAS will select a suitable operation for the de-raining task from the search space S. The mathematical expression is as follows:

$$O_n^1(I_n^1) = \sum_{m\epsilon I_n^1} \sum_{o\epsilon S} \frac{exp(\alpha_o^m)}{\Sigma_{o'\epsilon S} exp(\alpha_{o'}^m)} o(m) \quad (2)$$

where α_o^m denotes the structural weight of the topology of the cell, and the weight of each operation in the search space S is denoted using ω.

While searching the network, the training dataset is split into two parts. One part is utilized to search for the cell's topological weights, denoted as α. The other portion is employed to obtain the weights ω of all the operations within the search space S. The cell undergoes a topological search, followed by a weighted search of the search space.

Figure 4

The internal structure of the cell. I_n^1 and I_n^2 denote the inputs of the cell, Node denotes the operation inside the cell, and I_n denotes the output of the cell.

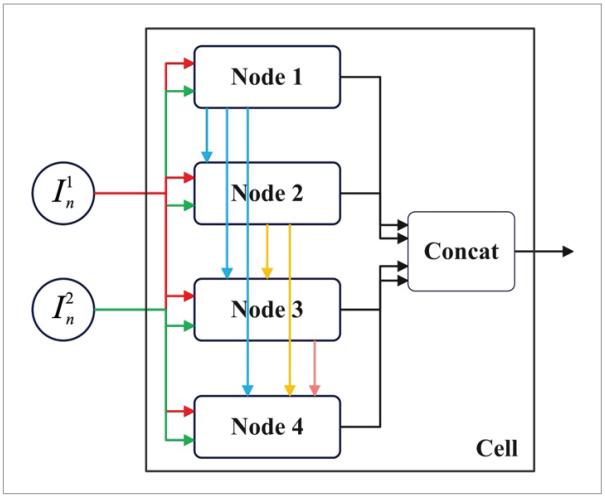

The search space encompasses all potential network structures that can be considered candidates. The GDAS search space is comprised of many convolutional and pooling layers. Nevertheless, conventional methods need to be improved for rain removal assignments due to their crucial role in restoring image details. Applying cascading convolutional kernels proves to be more efficient in removing rain [24]. Consequently, we modified the search space S for the rain removal task, as shown in Figure 5.

In our modified search space, we incorporated a variety of convolution operations with different kernel sizes (e.g., 5×5, 7×7, and 11×11) to enhance the model's ability to capture multi-scale rain streaks. Rain streaks appear in images in different shapes, directions, and scales. Therefore, larger convolutional kernels (7×7 and 11×11) can capture rain streaks and low-frequency information at larger scales, thereby processing more giant raindrops or rain streaks. Smaller convolutional kernels (such as 5×5 can extract local fine features and denoise fine rain streaks and high-frequency textures. This design ensures the network can process local details and broader contextual information, crucial for effectively removing rain from images. Additionally, we introduced dilated convolutions (DConv) in several layers to expand the receptive field without losing spatial resolution. This helps the network capture long-range dependencies, enabling it to process more complex rain patterns across varying image regions.

Moreover, we integrated residual connections in each operation block to improve gradient flow and maintain stable training, particularly in deeper architectures. The residual connections also help preserve image details during rain removal, essential for high-quality image restoration.

To further enhance the network's ability to focus on relevant features, we included the CBAM. This attention mechanism combines Channel Attention (CAM) and Spatial Attention (SAM), enabling the network to dynamically allocate more resources to significant regions, such as rain streaks while ignoring less important areas. This targeted attention further improves the rain removal performance by ensuring that the network prioritizes important visual features.

Figure 5

Our search space consists of seven operations: C53, C75, C117, DC53, DC75, DC117, and CBAM, where the prefix D denotes the dilated convolution, and CBAM is the attentional module with channel attention and spatial attention.

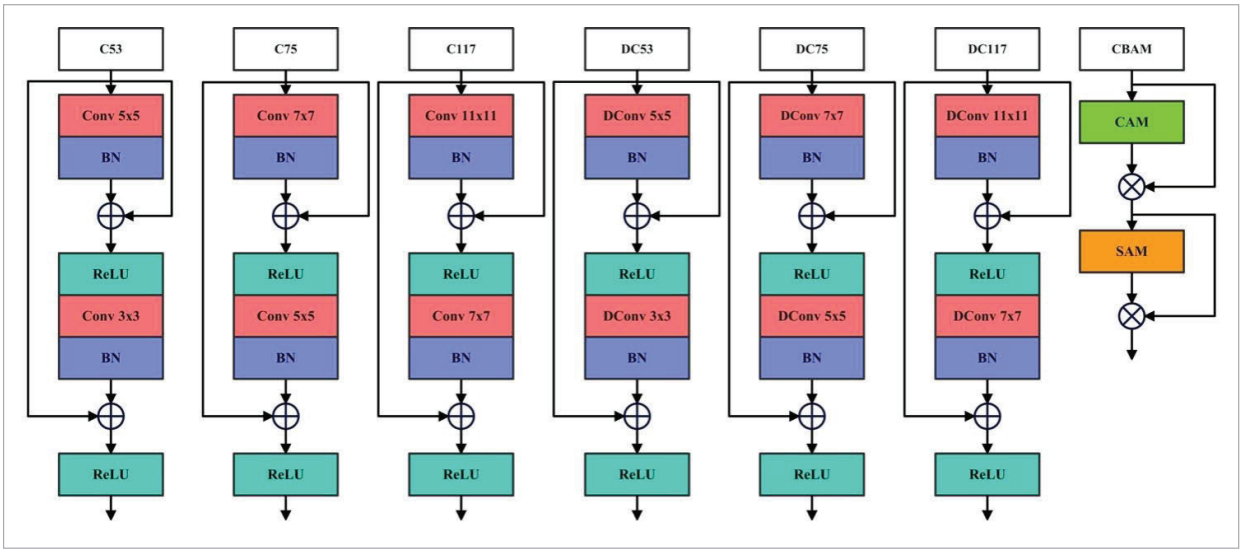

Overall, by enriching the search space with multi-scale convolutions, dilated convolutions, residual connections, and attention mechanisms, we have significantly improved the capacity of the NAS framework to generate architectures that excel in rain removal tasks. These modifications allow the search process to explore a broader, more effective range of network designs tailored to the unique challenges of image de-raining.

3.3. Simple Feature Fusion Method

The image features are divided into four components by the 2D DWT algorithm: X_{LL}, X_{LH}, X_{HL} and X_{HH}. X_{LL} contains all the structural information of the image, while X_{HH} preserves the detailed information of the image. X_{LH} and X_{HL} contain structure and detail information. The 2D-DWT is a simple feature fusion technique called Simple Feature Fusion (SFF). In this approach, only the X_{LL} and X_{HH} components are used for feature fusion. In contrast, the X_{LH} and X_{HL} components are replaced by zero feature components with the same dimensions as the original ones. The Residual Dense Block (RDB) technique is used to optimize the learning of complex features and the backpropagation of gradients to improve the quality of the image features. The RDB is an amalgamation of the Residual Network (ResNet) [9] and the Dense Connected Network (DenseNet) [11], integrating the benefits of both architectures. Residual connection mitigates the issue of gradient vanishing and enhances information flow, capturing greater image details. Conversely, dense connections enable the immediate transmission of feature maps from each layer to all subsequent layers within the network. This facilitates the network's integration of features across several levels, generating more potent features. RDB is frequently utilized for image restoration and single-image super-resolution (SISR) [50] activities. Mathematical expression is

$$\begin{aligned} X_F &= IDWT(LL, HH, HL_{zero}, LH_{zero}) \\ X_{RDB1} &= RDB(X_F) \\ X_{RDB2} &= RDB(X_{RDB1}) \\ X_{SFF} &= X_{RDB1} + X_{RDB2} + X_{SF} \end{aligned} \tag{3}$$

where LL and HH denote the feature components obtained by applying FSB, HL_{zero} and LH_{zero} are zero feature components, and X_{SFF} represents the shallow features in the RGB domain.

3.4. Image Reconstruction Network and Loss Function

A simple convolution operation is used to facilitate the remapping of image features and image resto-

ration within the image reconstruction network. Here is the mathematical expression:

$$R = Conv\left(BN\left(Conv\left(X_{SE}\right)\right)\right) \tag{4}$$

In the context of single-image de-raining tasks, employing L_1 and L_2 losses for network optimization is common practice. However, it is important to note that these loss functions operate at the pixel level. In this study, we aim to ensure that the restored image aligns with human judgment. To do this, we integrate the PSNR loss with the SSIM loss and incorporate the edge loss [44]. Here is the mathematical expression:

$$PSNR\left(I,G\right) = 20 \times \log_{10}\left(\frac{MAX_I}{\sqrt{MSE\left(I,G\right)}}\right) \tag{5}$$

where I represents the derained image, G represents the ground truth (GT) image, $MSE(I,G)$ denotes the mean square error between the derained image and the GT image and MAX_I denotes the maximum pixel value of the image.

$$SSIM\left(I,G\right) = \frac{\left(2\mu_I\mu_G + C_1\right)\left(2\sigma_I\sigma_G + C_2\right)}{\left(\mu_I^2 + \mu_G^2 + C_1\right)\left(\sigma_I^2\sigma_G^2 + C_2\right)} \tag{6}$$

where I represents the image after rain removal, G represents the GT image, and μ_I, μ_G, σ_I, and σ_G denote the mean and standard deviation of the input image. C_1 and C_2 are constants used to prevent division by zero.

$$\begin{aligned} &\mathrm{L}_{PS}\left(I_{clr}, I_{GT}\right) = \frac{1 - \mathrm{L}_{SSIM}\left(I_{clr}, I_{GT}\right)}{\mathrm{L}_{PSNR}\left(I_{clr}, I_{GT}\right) + \varepsilon} \\ &\mathrm{L}_{edge}\left(I_{clr}, I_{GT}\right) = \sqrt{\left|\Delta\left(I_{clr}\right) - \Delta\left(I_{GT}\right)\right|^2 + \omega^2} \\ &\mathrm{L}\left(I_{clr}, I_{GT}\right) = \mathrm{L}_{PS}\left(I_{clr}, I_{GT}\right) + \lambda \mathrm{L}_{edge}\left(I_{clr}, I_{GT}\right) \mathrm{Z} \end{aligned} \tag{7}$$

where $\mathrm{L}_{SSIM}(\cdot) \in [0,1]$ denotes the SSIM loss. $\mathrm{L}_{PSNR}(\cdot) \in [0,\infty)$ denotes the PSNR loss. $\Delta(\cdot)$ denotes the Laplace operation, and ϵ is a constant that ensures that the denominator of $\mathrm{L}_{PS}(\cdot)$ does not have a zero, and ω is also a constant.

In image restoration, a method that combines PSNR loss, SSIM loss, and edge loss significantly improves the quality of t he restored image, making up for the shortcomings of traditional L_1 and L_2 loss in terms of structure and detail preservation. PSNR focuses on global pixel errors to ensure overall fidelity; SSIM optimizes brightness, contrast, and structural similarity by simulating the human visual system to improve subjective quality; edge loss enhances high-frequency details, preserving sharp contours and textures to enhance visual appeal. This multi-objective optimization strategy balances the needs of pixel-level, structural-level, and high-frequency information to generate images that perform well in objective metrics (such as PSNR) and subjective evaluations (such as human perception). In addition, the method is simple to implement, the weights are adjustable, it adapts to multiple tasks (such as denoising and super-resolution), and it can be combined with advanced methods such as perceptual loss, making it highly flexible and extensible.

4. Experiments

In this section, we present a thorough assessment of WNASNet's efficacy. In this section, we describe the dataset and the assessment criteria employed in the comparative experiment. Next, we provide a detailed account of the experimental environment. Subsequently, we showcase the efficacy of WNASNet by using a blend of quantitative and qualitative methodologies. Following this, we proceed to verify the efficacy of each module within the WNASNet by the implementation of ablation experiments. Ultimately, the WNASNet is employed as a preliminary task for the target detection task, illustrating the WNASNet's efficacy in enhancing the subsequent performance.

4.1. Dataset and Evaluation Metrics

Synthetic datasets: We first introduce the synthetic datasets created specifically for training and testing de-raining algorithms. Synthetic datasets have become widely used in de-raining due to their ability to provide ground truth rain-free images for evaluation purposes. These datasets are generated by adding rain effects to clean, high-quality images.

One of the synthetic datasets used in our experiments is the Rain200L dataset [41]. It consists of 200 high-resolution images with different types and intensities of rain. This dataset is commonly used as

a benchmark for evaluating de-raining algorithms. The ground truth rain-free images are available for comparison during evaluation.

Another synthetic dataset used in our experiments is the Rain200H dataset [41]. It is an extension of the Rain200L dataset, containing 200 additional high-resolution images with more challenging rain patterns and intensities. Similarly, ground truth rain-free images are provided for evaluation.

Furthermore, we include the Rain800 [48] and Rain1400 [7] dataset, which contain 800 and 1400 rain images with diverse rain patterns and intensities, respectively. This dataset offers a more extensive evaluation framework to test de-raining algorithms' robustness and generalization capabilities.

Real-world datasets: In addition to synthetic datasets, we also include real-world datasets in our evaluation to assess the performance of our de-raining framework on more challenging and diverse rain images. Real-world datasets offer a realistic representation of rain in different scenes and capture the complexity and variability in natural rainy images.

One of the real-world datasets employed in our experiments is the MPID dataset [16], which consists of 185 high-resolution images obtained from various sources. These images depict different outdoor scenes with rain, including urban environments, countryside landscapes, and natural settings. The MPID dataset is widely used in the de-raining community to evaluate the performance of de-raining algorithms in real-world scenarios.

Furthermore, we incorporate the SPA dataset [37], which contains 146 real-world rain images captured from various viewpoints and angles. These images exhibit a wide range of rain intensities and patterns, making them suitable for testing the effectiveness of de-raining algorithms in diverse weather conditions.

To summarize, the real-world datasets utilized in our experiments include the MPID and SPA datasets. These datasets encompass a diverse collection of rain images captured in different environments and can provide insights into the real-world performance of our WNASNet.

Evaluation metrics: Evaluation metrics are crucial for assessing the effectiveness of de-raining models. Therefore, for synthetic datasets with paired images, we use PSNR [13] (the more significant the value, the better the image quality), SSIM [40] (the closer the value is to 1, the more similar the image structure), and LPIPS [49] (the closer the value is to 0, the closer the recovered image is to the reference image). We use NIQE [27] and BRISQUE [26] for real-world datasets, which indicate that the smaller the value, the better the image quality.

4.2. Implementation and Training Details

Search Configuration: We partitioned the training set D into two subsets: D_{train}, which comprises 70% of the data, and D_{val}, which includes the remaining 30%. The architectural parameters α, are optimized using the validation dataset, D_{val}, while the network parameters ω, are optimized using the training dataset D_{train}. Figure 2 displays the configuration of each FSB. Each block consists of a stack of N brain cells, and for our tests, we chose N=4 to accommodate the restrictions of GPU memory. The channel is configured to a value of 128. During the search process, we employ the Adam optimization algorithm to fine-tune the architecture parameters (α) and network parameters (ω). The starting learning rates for alpha and omega are set to 0.002 and 0.001, respectively. The batch size is 16, and the weight decay is 0.0005.

Train Configuration: Following an extensive search for robust architectures, we proceeded to train WNASNet for 200 epochs. We employed Adam as the optimizer, with a momentum value of 0.9 and a weight decay of 0.0005. The initial learning rate is configured at 0.001, and the training process incorporates the cosine annealing procedure. For both searching and training, we utilize a patch-based training technique [31] where we extract randomly cropped patches measuring 128×128 pixels from each image. Horizontal image flipping is a technique employed for data augmentation [30].

To verify the robustness of the proposed model, we used the same experimental settings and performed five model searches and training on the Rain200L dataset, with the results shown in Table 2. In these independent experiments, we found that the performance metrics searched for were consistent, with a standard deviation of 0.03 for PSNR and 0.002 for SSIM. The experiments show that our NAS method has good robustness and stability between different runs, as shown in Figure 6.

Figure 6
The difference in model performance after multiple searches and training.

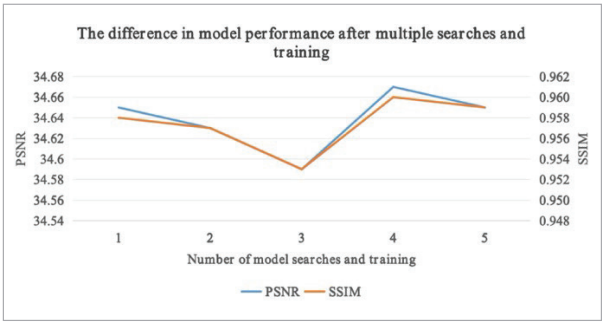

Table 2
Results after five independent model searches and training with the same experimental settings on the Rain200L dataset. The color **red** signifies the highest level of performance.

No.	PSNR	SSIM
1	34.65	0.958
2	34.63	0.957
3	34.59	0.953
4	34.67	0.960
5	34.64	0.959
Std Dev	0.03	0.002

4.3. Comparison with the State-of-the-Arts

We compared WNASNet with advanced approaches such as RCDNet, CCN, DRT, MWDCNN and MANAS. The open source code provided in the respective research papers was used to obtain the source code for all these methods. The benchmark dataset was used to re-execute all the source code. Table 3 presents the qualitative assessment of several techniques based on PSNR, SSIM and LPIPS metrics. The results show that our designed WNASNet network has significant PSNR, SSIM and LPIPS metrics advantages. It exhibits the highest performance on all datasets except the Rain800 dataset, where WNASNet also ranks first in PSNR metrics and second in SSIM metrics. The quantitative analysis results confirm the effectiveness of the WNASNet network in removing rain streaks from a single image.

Results on synthetic datasets. Figure 7 illustrates the qualitative assessment of seven rain removal techniques on four samples derived from the Rain200L dataset. The figure demonstrates that the utilization of HiNAS for rain streak removal results in a general alteration of the image colours. Additionally, the model exhibits limited proficiency in restoring image details, impacting the efficacy of rain removal from the image. CCN effectively eliminates the majority of the streaks. However, it fails to capture the picture edge information, resulting in an incomplete recovered image. While RCDNet can mitigate certain rain streaks, it exhibits artefacts when confronted with intense rain streaks, limiting the model's ability to remove rain effectively. MANAS is a de-raining model that is derived from NAS. It effectively eliminates the majority of rain streaks but cannot eliminate the thicker or thinner rain streaks. As a result, numerous rain streaks persist after the image has been de-rained. MWDCNN exhibits robust resilience against rain but at the expense of certain image

Table 3
The PSNR and SSIM results of several rain removal techniques are evaluated on four synthetic datasets. The color **red** signifies the highest level of performance, while the color **blue** signifies the second highest level.

Methods	Rain200L			Rain200H			Rain800			Rain1400		
	PSNR	SSIM	LPIPS	PSNR	SSIM	LPIPS	PSNR	SSIM	LPIPS	PSNR	SSIM	LPIPS
HiNAS	30.88	0.935	0.082	26.31	0.869	0.082	23.04	0.781	0.172	27.07	0.857	0.126
RCDNet	29.91	0.917	0.130	24.64	0.829	0.129	22.36	0.743	0.180	20.07	0.774	0.210
CCN	32.94	0.950	0.049	26.12	0.860	0.098	24.71	0.842	0.159	28.51	0.900	0.120
DRT	30.26	0.879	0.096	24.54	0.740	0.132	21.66	0.658	0.189	26.44	0.778	0.204
MWDCNN	34.27	0.900	0.021	28.86	0.837	0.068	25.73	0.812	0.066	29.28	0.816	0.101
MANAS	32.57	0.957	0.056	26.24	0.866	0.094	24.38	0.845	0.167	28.52	0.901	0.114
Ours	34.67	0.960	0.012	29.25	0.871	0.055	25.82	0.823	0.057	29.37	0.906	0.026

Figure 7

From (a) to (g), the qualitative comparisons of different rain removal models on the Rain200L dataset are shown. The color **red** indicates the best performance, while the color **blue** indicates the second best performance.

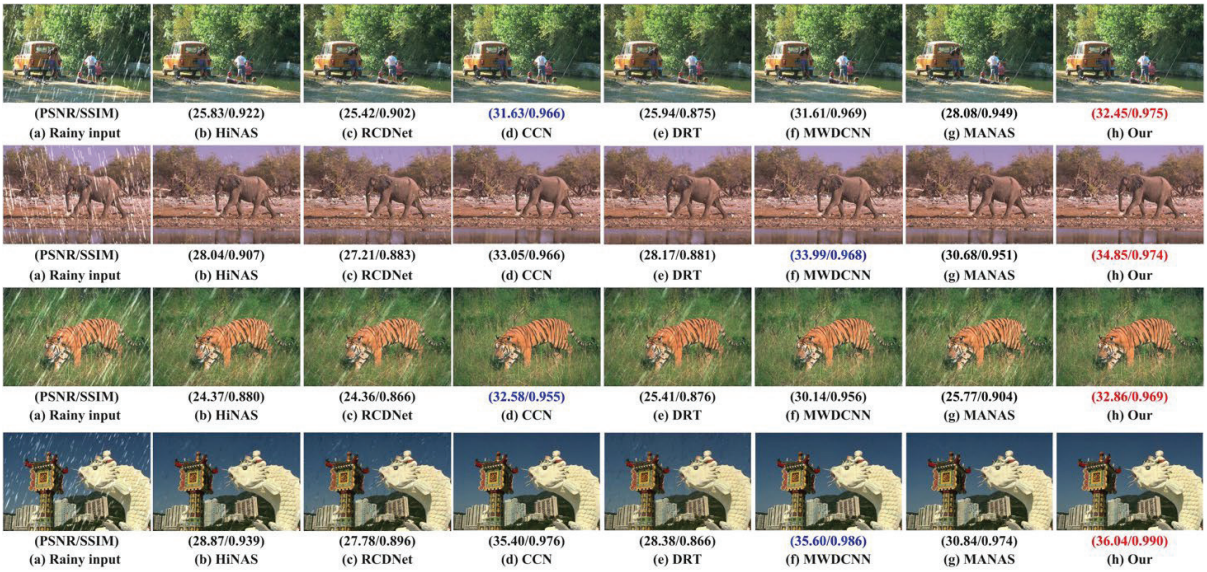

Figure 8

Real images taken in rainy conditions are compared qualitatively. The color **red** represents the highest level of performance, and the color **blue** symbolizes the second position.

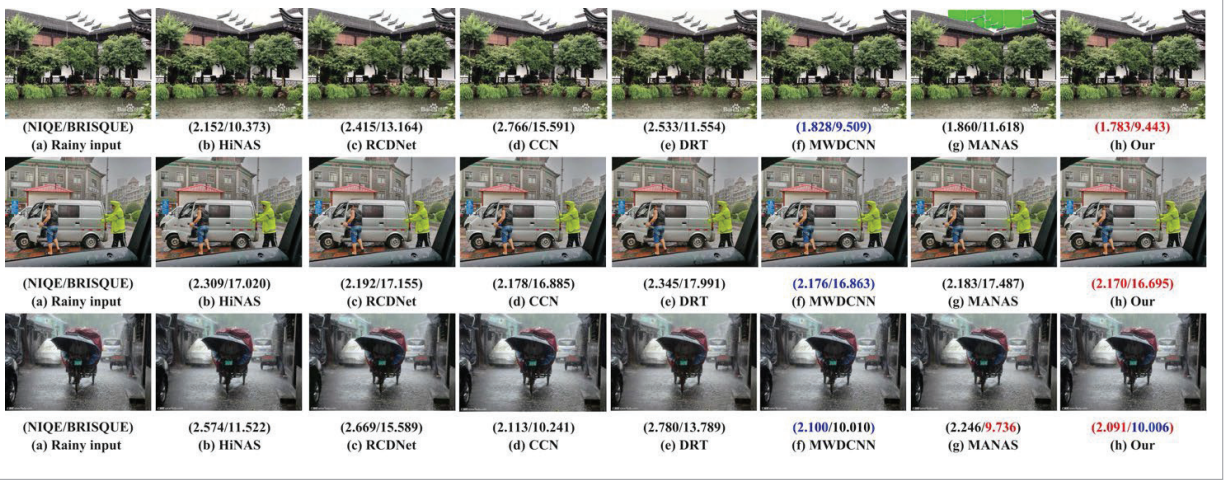

intricacies. Multi-tasking image restoration models, known as DRT, exhibit variations in their single-task performance compared to state-of-the-art models. In contrast to the existing state-of-the-art (SOTA) approaches, our proposed WNASNet can effectively eliminate rain streaks of varying densities.

Furthermore, the rain removal outcomes of WNASNet exhibit enhanced colour vibrancy and more intricate structural data, rendering them more advantageous compared to alternative rain removal techniques. Higher PSNR and lower LPIPS scores indicate a superior ability to reconstruct rain-free images with finer detail preservation and overall image quality would help clarify the metrics' importance.

Results on a real-world dataset. Table 4 shows the results of evaluating multiple models using the NIQE and BRISQUE metrics on the MPID and SPA datasets. Figure 8 shows the results of various de-raining techniques applied to three actual rainy day samples. The findings in Figure 7 show that the images continue to exhibit rain streaks even after undergoing the de-raining process using MWDCNN. The rain streaks could not be eliminated by DRT, CCN, and HiNAS, leading to reconstructed images needing improvement in essential details. MANAS cannot remove rain streaks and accurately preserve the structural elements of an image in real-world de-raining situations. An error occurred during the processing of the image texture by RCDNet. WNASNet demonstrates exceptional de-raining abilities, effectively removing rain streaks and preserving detailed details in image reconstruction.

4.4. Ablation Study

We performed experiments in Table 5 and Figure 9, where we methodically eliminated particular components from our framework. This allowed us to observe each component's effect on the de-raining algorithm's overall performance. We evaluated the rain removal results of different WNASNet based on PSNR and SSIM metrics.

We first constructed a basic model V_0 without NAS or wavelet transform and used L_1 loss. Then, we analyzed the effect of incorporating wavelet transform into the model on the rain removal effect. By adding a wavelet transform to the V_0 model while keeping the other variables of the basic model unchanged, we increased the utilization of multi-scale information in the wavelet transform. The results of the study show that the addition of the wavelet transform significantly improves the performance of the model. Specifically, the PSNR value of the model using wavelet transform is enhanced by about 0.2 compared with the V_0 model. This shows that wavelet transform is crucial in improving the rain removal process, enabling the model to capture and process multi-scale features, which is essential for accurately detecting and removing rain marks of various sizes.

Next, we also evaluated the model's performance after adding the NAS and wavelet transform components. Compared with the V_1 model, the PSNR improved by about 0.2. This confirms that NAS significantly contributes to the effectiveness of the rain removal algorithm.

In addition to the architectural components, we investigated the influence of the loss function on the de-raining results. We compared two different loss functions:

L_1 Loss Function: We trained the model using the traditional L_1 loss function, focusing on minimizing the pixel-wise differences between the de-rained image and the ground truth. This is a commonly used loss function in image restoration tasks.

Composite Loss Function (PSNR, SSIM, and Edge Loss): We employed a composite loss function that combines PSNR, SSIM, and edge loss. This loss function is designed to enhance the perceptual quality of the de-rained images by not only considering pixel-wise accuracy but also structural similarity and edge preservation.

The experimental results demonstrated that using the composite loss function significantly improved de-raining performance compared to using the L_1 loss alone. Models trained with the composite loss func-

Table 4

The NIQE and BRISQUE scores of various rain removal techniques on the two real-world datasets. The color **red** signifies the highest level of performance, while the color **blue** symbolizes the second position.

Methods	MPID		SPA	
	NIQE	BRISQUE	NIQE	BRISQUE
HiNAS	3.381	27.572	4.647	26.620
RCDNet	3.300	25.379	4.693	**24.753**
CCN	3.074	24.913	4.568	26.998
DRT	3.285	**24.654**	**4.385**	24.768
MWDCNN	**3.057**	24.688	4.410	26.174
MANAS	3.111	24.803	4.394	26.128
Ours	**3.016**	**24.437**	**4.221**	**24.653**

Table 5

Ablation experiments with local search networks on the Rain200L dataset.

Variants	WT	NAS	L_1	L_{our}	PSNR	SSIM
V_0	w/o	w/o	√	w/o	34.17	0.951
V_1	√	w/o	√	w/o	34.38	0.955
V_2	√	√	√	w/o	34.58	0.958
V_3	√	√	w/o	√	34.67	0.960

Figure 9
Results of the visual ablation experiments. (a) Rainy image, (b) result of the V_0 network, (c) result of the V_1 network, (d) result of the V_2 network, (e) result of the V_3 network.

tion achieved higher PSNR and SSIM scores and produced images with better visual quality and more preserved details. Specifically, there was an improvement of about 0.09 in PSNR when using the composite loss function over the L_1 loss. This indicates that optimizing the model with respect to multiple criteria related to image quality leads to superior de-raining results.

4.4. Application

To illustrate the efficacy of our WNASNet in enhancing the performance of high-level vision applications, we initially conducted a de-raining operation on the rain images inside the RID dataset, employing the de-raining model. Subsequently, the YOLOv5 model was used to detect objects on 100 image sets inside the RID dataset. The results of the detection process are visually presented in Figure 10. The figure demonstrates a substantial enhancement in the confidence and accuracy of item detection following the de-raining process compared to the pre-de-raining procedure.

5. Conclusion

This research presents insights from experimental findings using our proposed Wavelet-Enhanced NAS architecture for single-image de-raining. The performance comparison unequivocally illustrates the superiority of our process in contrast to existing de-raining techniques. In addition, the ablation study offers a comprehensive investigation of the individual contributions made by various components within our system. The visualization of the de-raining findings clearly demonstrates our method's efficacy in eliminating rain streaks while retaining crucial image features. In summary, the experimental results significantly confirm the efficiency of our suggested approach and emphasize its potential for practical use in removing rain from single images.

Based on this research, the model's performance can be further improved in the future by exploring different types of search space. At the same time, knowledge distillation is also a very good research direction. Knowledge distillation on large vision-based models can remove rain streaks of different types.

Acknowledgement

This research is currently being generously supported by several projects. These include the the Jiangsu Province's Research Project on Basic Sciences (Natural Sciences) in Colleges and Universities (24KJA520007), and the Team Foundation of Jiangsu Provincial Department of Education (2022.13).

Figure 10
Experimental results of the image rain removal model in downstream object detection tasks. The results show that the WNASNet proposed in this study can significantly improve the performance of downstream tasks and provide higher-quality image inputs for downstream tasks.

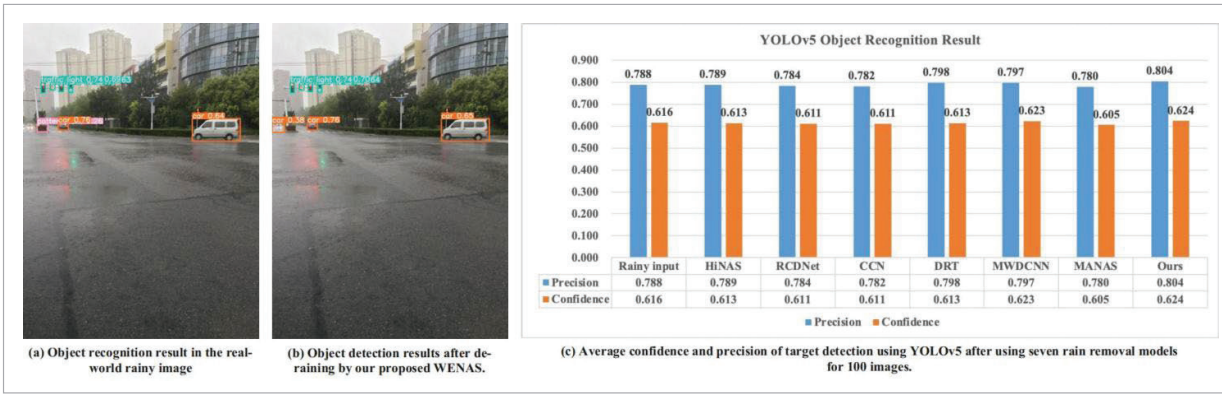

(a) Object recognition result in the real-world rainy image

(b) Object detection results after de-raining by our proposed WENAS.

(c) Average confidence and precision of target detection using YOLOv5 after using seven rain removal models for 100 images.

References

1. Cai, L., Fu, Y., Huo, W., Xiang, Y., Zhu, T., Zeng, H., Zeng. D. Multiscale Attentive Image De Raining Networks via Neural Architecture Search. IEEE Transactions on Circuits and Systems for Video Technology, 2022, 33(2), 618-633. https://doi.org/10.1109/TCSVT.2022.3207516
2. Cheng, G., Matsune, A., Du, H., Liu, X., Zhan, S. Exploring More Diverse Network Architectures for Single Image Super Resolution. Knowledge Based Systems, 2022, 235, 107648. https://doi.org/10.1016/j.knosys.2021.107648
3. Dong, X., Yang, Y. Searching for a Robust Neural Architecture in Four GPU Hours. IEEE Conference on Computer Vision and Pattern Recognition, 2019, 1761-1770. https://doi.org/10.1109/CVPR.2019.00186
4. Dosovitskiy, A., Beyer, L., Kolesnikov, A., Weissenborn, D., Zai, X., Unterthiner, T., Dehghami, M., Minderer, M., Heigold, G., Gelly, S., Uszkoreit, J., Houlsby, N. An Image Is Worth 16x16 Words: Transformers for Image Recognition at Scale. 9th International Conference on Learning Representations, 2021.
5. Du, S., Liu, Y., Ye, M., Xu, Z., Li, J., Liu, J. Single Image Deraining via Decorrelating the Rain Streaks and Background Scene in Gradient Domain. Pattern Recognition, 2018, 79, 303-317. https://doi.org/10.1016/j.patcog.2018.02.016
6. Fu, J., Hou, C., Chen, Z. AutoDerain: Memory Efficient Neural Architecture Search for Image Deraining. 2021 International Conference on Visual Communications and Image Processing (VCIP), 2021, 1-5. https://doi.org/10.1109/VCIP53242.2021.9675339
7. Fu, X., Huang, J., Zeng, D., Huang, Y., Ding, X., Paisley, J. W. Removing Rain from Single Images via a Deep Detail Network. 2017 IEEE Conference on Computer Vision and Pattern Recognition, 2017, 1715-1723. https://doi.org/10.1109/CVPR.2017.186
8. Fu, X., Liang, B., Huang, Y., Ding, X., Paisley, J. W. Lightweight Pyramid Networks for Image Deraining. IEEE Transactions on Neural Networks and Learning Systems, 2020, 31(6), 1794-1807. https://doi.org/10.1109/TNNLS.2019.2926481
9. He, K., Zhang, X., Ren, S., Sun, J. Deep Residual Learning for Image Recognition. 2016 IEEE Conference on Computer Vision and Pattern Recognition, 2016, 770-778. https://doi.org/10.1109/CVPR.2016.90
10. Hsu, W.-Y., Jian, P.-W. Detail Enhanced Wavelet Residual Network for Single Image Super Resolution. IEEE Transactions on Instrumentation and Measurement, 2022, 71, 1-13. DOI: 10.1109/TIM.2022.3192280. https://doi.org/10.1109/TIM.2022.3192280
11. Huang, G., Liu, Z., van der Maaten, L., Weinberger, K. Q. Densely Connected Convolutional Networks. 2017 IEEE Conference on Computer Vision and Pattern Recognition (CVPR), 2017, 2261-2269. https://doi.org/10.1109/CVPR.2017.243
12. Huang, Y., Huang, J., Liu, J., Yan, M., Dong, Y., Lv, J., Chen, C., Chen, S. WaveDM: Wavelet Based Diffusion Models for Image Restoration. IEEE Transactions on Multimedia, 2024, 26, 7058-7073. DOI: 10.1109/TMM.2024.3359769. https://doi.org/10.1109/TMM.2024.3359769
13. Huynh Thu, Q., Ghanbari, M. Scope of Validity of PSNR in Image/Video Quality Assessment. Electronics Letters, 2008, 44(13), 800-801. https://doi.org/10.1049/el:20080522
14. Kim, J.-H., Lee, C., Sim, J.-Y., Kim, C.-S. Single Image Deraining Using an Adaptive Nonlocal Means Filter. IEEE International Conference on Image Processing (ICIP), 2013, 914-917. https://doi.org/10.1109/ICIP.2013.6738189
15. Lee, B., Ko, K., Hong, J., Ko, H. Single Cell Training on Architecture Search for Image Denoising. arXiv Preprint, 2022, arXiv:2212.06368.
16. Li, S., Araujo, I. B., Ren, W., Wang, Z., Tokuda, E. K., Hirata Junior, R., Cesar-Junior, R., Zhang, J., Guo, X., Cao, X. Single Image Deraining: A Comprehensive Benchmark Analysis. IEEE Conference on Computer Vision and Pattern Recognition, 2019, 3838-3847. https://doi.org/10.1109/CVPR.2019.00396
17. Li, X., Wu, J., Lin, Z., Liu, H., Zha, H. Recurrent Squeeze And Excitation Context Aggregation Net for Single Image Deraining. In: Ferrari, V., Hebert, M., Sminchisescu, C., Weiss, Y. (Eds.) Computer Vision - ECCV 2018. Lecture Notes in Computer Science, vol. 11211. Springer, 2018, 262-277. https://doi.org/10.1007/978-3-030-01234-2_16
18. Li, Z., Chen, X., Guo, S.-N., Wang, S., Pun, C.-M. WavEnhancer: Unifying Wavelet and Transformer for Image Enhancement. Journal of Computer Science and Technology, 2024, 39(2), 336-345. DOI: 10.1007/S11390 024 3414 Z. https://doi.org/10.1007/s11390-024-3414-z
19. Liang, Y., Anwar, S., Liu, Y. DRT: A Lightweight Single Image Deraining Recursive Transformer. IEEE/CVF Conference on Computer Vision and Pattern Recognition Workshops, 2022, 588-597. DOI: 10.1109/

CVPRW56347.2022.00074. https://doi.org/10.1109/CVPRW56347.2022.00074

20. Liu, C., Zoph, B., Neumann, M., Shlens, J., Hua, W., Li, L.-J., Fei-Fei, L., Yuille, A., Huang, J., Murphy, K. Progressive Neural Architecture Search. In: Ferrari, V., Hebert, M., Sminchisescu, C., Weiss, Y. (Eds.) Computer Vision - ECCV 2018. Lecture Notes in Computer Science, vol. 11205. Springer, 2018, 19-35. https://doi.org/10.1007/978-3-030-01246-5_2
21. Liu, H., Simonyan, K., Vinyals, O., Fernando, C., Kavukcuoglu, K. Hierarchical Representations for Efficient Architecture Search. 6th International Conference on Learning Representations, 2018.
22. Liu, H., Simonyan, K., Yang, Y. DARTS: Differentiable Architecture Search. 7th International Conference on Learning Representations, 2019.
23. Liu, P., Zhang, H., Zhang, K., Lin, L., Zuo, W. Multi Level Wavelet CNN for Image Restoration. IEEE Conference on Computer Vision and Pattern Recognition Workshops, 2018, 773-782. https://doi.org/10.1109/CVPRW.2018.00121
24. Liu, X., Suganuma, M., Sun, Z., Okatani, T. Dual Residual Networks Leveraging the Potential of Paired Operations for Image Restoration. IEEE Conference on Computer Vision and Pattern Recognition, 2019, 7007-7016. https://doi.org/10.1109/CVPR.2019.00717
25. Luo, Y., Xu, Y., Ji, H. Removing Rain from a Single Image via Discriminative Sparse Coding. IEEE International Conference on Computer Vision, 2015, 3397-3405. https://doi.org/10.1109/ICCV.2015.388
26. Mittal, A., Moorthy, A. K., Bovik, A. C. No Reference Image Quality Assessment in the Spatial Domain. IEEE Transactions on Image Processing, 2012, 21(12), 4695-4708. https://doi.org/10.1109/TIP.2012.2214050
27. Mittal, A., Soundararajan, R., Bovik, A. C. Making a 'Completely Blind' Image Quality Analyzer. IEEE Signal Processing Letters, 2013, 20(3), 209-212. https://doi.org/10.1109/LSP.2012.2227726
28. Monika, R., Rao, Y. R. Rainy Image Enhancement Using Modified Multistage Gaussian Filter and Weighted Median Guided Filter. 2020 4th International Conference on Computer, Communication and Signal Processing (ICCCSP), 2020, 1-7. https://doi.org/10.1109/ICCCSP49186.2020.9315225
29. Quan, R., Yu, X., Liang, Y., Yang, Y. Removing Raindrops and Rain Streaks in One Go. IEEE Conference on Computer Vision and Pattern Recognition, 2021, 9147-9156. https://doi.org/10.1109/CVPR46437.2021.00903
30. Quan, Y., Deng, S., Chen, Y., Ji, H. Deep Learning for Seeing Through Window with Raindrops. IEEE/CVF International Conference on Computer Vision (ICCV), 2019, 2463-2471. https://doi.org/10.1109/ICCV.2019.00255
31. Ren, D., Zuo, W., Hu, Q., Zhu, P., Meng, D. Progressive Image Deraining Networks: A Better and Simpler Baseline. IEEE Conference on Computer Vision and Pattern Recognition, 2019, 3937-3946. https://doi.org/10.1109/CVPR.2019.00406
32. Shen, Y., Wei, M., Wang, Y., Fu, X., Qin, J. Rethinking Real World Image Deraining via an Unpaired Degradation Conditioned Diffusion Model. arXiv Preprint, 2023, arXiv:2301.09430.
33. Suganuma, M., Ozay, M., Okatani, T. Exploiting the Potential of Standard Convolutional Autoencoders for Image Restoration by Evolutionary Search. In: Dy, J. G., Krause, A. (Eds.), Proceedings of the 35th International Conference on Machine Learning. Proceedings of Machine Learning Research, vol. 80. PMLR, 2018, 4778-4787.
34. Tao, W., Yan, X., Wang, Y., Wei, M. MFFDNet: Single Image Deraining via Dual Channel Mixed Feature Fusion. IEEE Transactions on Instrumentation and Measurement, 2024, 73, 1-13. https://doi.org/10.1109/TIM.2023.3346498
35. Tian, C., Zheng, M., Zuo, W., Zhang, B., Zhang, Y., Zhang, D. Multi Stage Image Denoising with the Wavelet Transform. Pattern Recognition, 2023, 134, 109050. https://doi.org/10.1016/j.patcog.2022.109050
36. Wang, H., Xie, Q., Zhao, Q., Li, Y., Liang, Y., Zheng, Y., Meng, D. RCDNet: An Interpretable Rain Convolutional Dictionary Network for Single Image Deraining. IEEE Transactions on Neural Networks and Learning Systems, 2023. https://doi.org/10.1109/TNNLS.2022.3231453
37. Wang, T., Yang, X., Xu, K., Chen, S., Zhang, Q., Lau, R. W. H. Spatial Attentive Single Image Deraining with a High Quality Real Rain Dataset. IEEE Conference on Computer Vision and Pattern Recognition, 2019, 12270-12279. https://doi.org/10.1109/CVPR.2019.01255
38. Wang, Y., Yan, X., Wang, F. L., Xie, H., Yang, W., Zhang, X. P., Qin, J., Wei, M. UCL Dehaze: Toward Real World Image Dehazing via Unsupervised Contrastive Learning. IEEE Transactions on Image Processing, 2024, 33, 1361-1374. https://doi.org/10.1109/TIP.2024.3362153
39. Wang, Y., Liu, S., Chen, C., Zeng, B. A Hierarchical Approach for Rain or Snow Removing in a Single

Color Image. IEEE Transactions on Image Processing, 2017, 26(8), 3936-3950. https://doi.org/10.1109/TIP.2017.2708502

40. Wang, Z., Bovik, A. C., Sheikh, H. R., Simoncelli, E. P. Image Quality Assessment: From Error Visibility to Structural Similarity. IEEE Transactions on Image Processing, 2004, 13(4), 600-612. https://doi.org/10.1109/TIP.2003.819861
41. Yang, W., Tan, R. T., Feng, J., Liu, J., Guo, Z., Yan, S. Deep Joint Rain Detection and Removal from a Single Image. IEEE Conference on Computer Vision and Pattern Recognition, 2017, 1685-1694. https://doi.org/10.1109/CVPR.2017.183
42. Yang, W., Tan, R. T., Wang, S., Fang, Y., Liu, J. Single Image Deraining: From Model Based to Data Driven and Beyond. IEEE Transactions on Pattern Analysis and Machine Intelligence, 2021, 43(11), 4059-4077. https://doi.org/10.1109/TPAMI.2020.2995190
43. Ye, P., Li, B., Li, Y., Chen, T., Fan, J., Ouyang, W. Beta DARTS: Beta Decay Regularization for Differentiable Architecture Search. IEEE Conference on Computer Vision and Pattern Recognition, 2022, 10864-10873. https://doi.org/10.1109/CVPR52688.2022.01060
44. Yin, X., Tu, G., Chen, Q. Multiscale Depth Fusion with Contextual Hybrid Enhancement Network for Image Dehazing. IEEE Transactions on Instrumentation and Measurement, 2023. https://doi.org/10.1109/TIM.2023.3318748
45. You, S., et al. Fine Perceptive GANs for Brain MR Image Super Resolution in Wavelet Domain. IEEE Transactions on Neural Networks and Learning Systems, 2023, 34(11), 8802-8814. DOI: 10.1109/TNNLS.2022.3153088. https://doi.org/10.1109/TNNLS.2022.3153088
46. Zhang, H., Li, Y., Chen, H., Gong, C., Bai, Z., Shen, C. Memory Efficient Hierarchical Neural Architecture Search for Image Restoration. International Journal of Computer Vision, 2022, 1-22. https://doi.org/10.1007/s11263-021-01537-w
47. Zhang, H., Li, Y., Chen, H., Shen, C. Memory Efficient Hierarchical Neural Architecture Search for Image Denoising. IEEE Conference on Computer Vision and Pattern Recognition, 2020, 3654-3663. https://doi.org/10.1109/CVPR42600.2020.00371
48. Zhang, H., Sindagi, V., Patel, V. M. Image De Raining Using a Conditional Generative Adversarial Network. IEEE Transactions on Circuits and Systems for Video Technology, 2020, 30(11), 3943-3956. https://doi.org/10.1109/TCSVT.2019.2920407
49. Zhang, R., Isola, P., Efros, A. A., Shechtman, E., Wang, O. The Unreasonable Effectiveness of Deep Features as a Perceptual Metric. IEEE Conference on Computer Vision and Pattern Recognition, 2018, 586-595. DOI: 10.1109/CVPR.2018.00068. https://doi.org/10.1109/CVPR.2018.00068
50. Zhang, Y., Tian, Y., Kong, Y., Zhong, B., Fu, Y. Residual Dense Network for Image Super Resolution. IEEE Conference on Computer Vision and Pattern Recognition, 2018, 2472-2481. https://doi.org/10.1109/CVPR.2018.00262
51. Zhang, Z., Wei, Y., Zhang, H., Yang, Y., Yan, S., Wang, M. Data Driven Single Image Deraining: A Comprehensive Review and New Perspectives. Pattern Recognition, 2023, 109740. https://doi.org/10.1016/j.patcog.2023.109740
52. Zoph, B., Le, Q. V. Neural Architecture Search with Reinforcement Learning. 5th International Conference on Learning Representations, 2017.